Reversible Switching of InP Nanowire Growth Direction by Catalyst Engineering

Jia Wang,[†] Sébastien R. Plissard,[†,‡] Marcel A. Verheijen,[†,§] Lou-Fé Feiner,[†] Alessandro Cavalli,[†] and Erik P. A. M. Bakkers*[,†,‡]
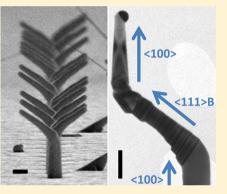
[†]Department of Applied Physics, Eindhoven University of Technology, 5600 MB Eindhoven, The Netherlands
[‡]Kavli Institute of Nanoscience, Delft University of Technology, 2600 GA Delft, The Netherlands
[§]Philips Innovation Services Eindhoven, 5656 AE Eindhoven, The Netherlands

S Supporting Information

ABSTRACT: We demonstrate high yield vapor–liquid–solid (VLS) growth of ⟨100⟩-oriented InP nanowire arrays. The highest yield (97%) is obtained when the catalyst droplet is filled with indium prior to nanowire nucleation to the equilibrium composition during nanowire growth. Using these ⟨100⟩ wires as a template we can reversibly switch between a ⟨100⟩ and a ⟨111⟩ growth direction by varying the indium content of the droplet. Modeling VLS growth by a kinetic nucleation model indicates that the growth direction is governed by the liquid–vapor interface energy that is strongly affected by the indium concentration in the catalyst droplet.

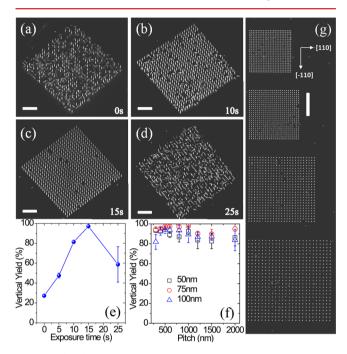**KEYWORDS:** Semiconductor nanowires, indium phosphide, VLS, catalyst engineering, growth direction

The III–V semiconductor nanowires are attractive as ideal building blocks for various nanoscale devices[1−5] and have been fabricated by many groups using different growth methods.[6−8] According to these studies, nanowires are generally grown in the ⟨111⟩B crystal direction; while other low-index growth directions have been occasionally reported.[9−23] Givargizov[19] first reported the ⟨100⟩ nanowire growth direction for gallium arsenide (GaAs) by the vapor–liquid–solid (VLS)[6] mechanism using Au particles as catalyst in 1975, and in the past decade nanowires of both indium phosphide (InP) and indium arsenide (InAs) have been grown in a ⟨100⟩ crystal direction.[20−23] All these ⟨100⟩ nanowires are defect-free and adopt a pure zincblende (ZB) crystal structure contrary to the standard ZB/WZ (Wurtzite) mixed structures observed for most of the ⟨111⟩B nanowires. Controlling the growth direction thus opens a new possibility to obtain pure crystal phase nanowires. An additional important advantage of ⟨100⟩ nanowires is that (100) orientated substrates have been mostly used in industry. Vertical nanowire growth on (100) substrates could thus combine the advanced properties of nanowires with current device processing technology. Moreover, it is important to understand the mechanism determining the nanowire growth direction. Currently, growth direction control within a single nanowire has been studied for group IV nanowires[24,25] but is still challenging for III/V materials.

In a previous study, we have investigated a broad range of nanowire growth parameters and we obtained a yield up to 56% of wires growing in the ⟨100⟩ direction.[23] Here, we report on a new method to control the growth direction of InP nanowires and demonstrate much higher yields. In addition, we show that by changing the catalyst shape in situ, we can controllably switch the growth direction between ⟨100⟩ and ⟨111⟩.

We first focus on optimizing the yield of ⟨100⟩ InP nanowires. Since the nanowire site control is essential for applications, such as optimizing light absorption in solar cells,[26] the following two lithography techniques were used to predefine the nanowire position on an InP (100) substrate: electron beam lithography (EBL) to fabricate small arrays with various pitches and diameters,[27] and nanoimprint (NI) to pattern large-scale areas.[28] The growth conditions are essentially the same as for our previously studied ⟨100⟩ InP nanowire arrays[23] (see Supporting Information S1 for more details). In order to further increase the yield of wires growing in the ⟨100⟩ direction, the droplet shape and composition were optimized, in analogy to optimizing the growth of ⟨111⟩ oriented GaAs nanowires on Si[29] by exposing them to trimethylindium (TMI) before nanowire growth was initiated. When the system reached the growth temperature of 440 °C under a phosphine (PH$_3$) flow, we simultaneously switched PH$_3$ off and TMI on. After exposure of the Au particle to TMI for 0 to 25 s, the PH$_3$ flux was turned on and the nanowire growth started. The yield of vertical ⟨100⟩ nanowires was

determined as a function of the exposure time by using scanning electron microscopy (SEM). For each sample, 5 EBL-patterned fields of 25 × 25 wires from different locations were measured. Upon increasing the exposure time from 0 to 15 s, the vertical yield increases from $27 \pm 1\%$ to $97 \pm 1\%$ (Figure 1a–c) and then decreases to $59 \pm 18\%$ at 25 s (Figure 1d). The

Figure 1. (a–d) SEM images at 30° tilt, showing InP nanowires grown on a InP (100) substrate with different TMI exposure times from 0 to 25 s before wire nucleation. The nanowire growth is catalyzed by gold particles with 75 nm diameter and 800 nm wire-to-wire distance, patterned by electron beam lithography. (e) The yield of vertical ⟨100⟩ nanowires versus exposure time. (f) The vertical yield for various wire diameters versus wire-to-wire distance for 15 s TMI exposure. (g) Topview SEM images showing InP nanowire arrays grown from 75 nm diameter Au particles with 15 s exposure time and wire-to-wire distances of 500, 600, 800, and 1000 nm (from top to bottom). The scale bars are 5 μm.

maximum is reached at 15 s, as shown in Figure 1e, and in this case the yield is mainly limited by missing wires, which could be due to an imperfect lithography process or to wires which have not nucleated. Nanowire arrays from different areas of the wafer were investigated and no significant trend of the vertical yield with wire diameter or wire-to-wire distance was found as shown in Figure 1f. In the topview SEM image in Figure 1g, there are four nanowire fields of 75 nm diameter gold particles and varying wire-to-wire distance from 500 to 1000 nm showing near-perfect vertical yield and uniformity.

In order to understand the influence of the droplet preconditioning on the nanowire growth direction, InP (100) wafers were patterned using nanoimprint with gold islands of 136 nm in diameter, 11 nm in height and droplet interdistances of 513 nm. These samples were heated to the growth temperature in the reactor and exposed to TMI for different periods but instead of starting the nanowire growth afterwards, the samples were cooled down quickly under H_2, cleaved, and measured by SEM. As it can be seen from the side-view SEM images in Figure 2a both the contact angle with the substrate, α, and the diameter of the catalyst droplet, $2r$, change significantly during the first 5 s, while for longer exposure times the changes
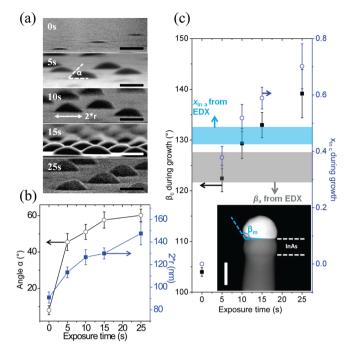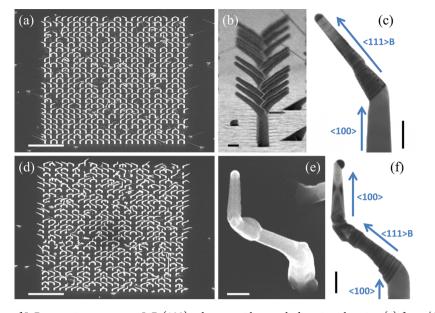

Figure 2. (a) SEM images of catalyst droplets for different TMI exposure times from 0 to 25 s viewed with substrate 88° tilted. The scale bars are 100 nm. The variation of the droplet density for varying exposure time occurs because the Au arrays patterned by nanoimprint are not aligned to the substrate crystal direction while the cleaving side facet is always (110). (b) Contact angle α and diameter $2r$ of the Au–In catalyst droplet versus exposure time, as obtained from combination of SEM and atomic force microscopy (AFM) measurements. (c) Contact angle of the droplet-nanowire interface β and indium fraction x_{In} in the catalyst droplet during nanowire growth versus TMI exposure time: (i) β_c (filled squares) and $x_{In,c}$ (open circles) calculated from the pregrowth data in (b); (ii) postgrowth, β_a (gray band), and $x_{In,a}$ (blue band) measured using energy-dispersive X-ray spectroscopy (EDX). The inset shows a ⟨100⟩ InP nanowire cooled down under AsH_3 with InAs top segment. The white dashed line indicates the position of the InAs segment and β_m the droplet-nanowire contact angle after growth. The scale bar is 50 nm.

are less pronounced (Figure 2b). During the exposure, the gold islands are filled with indium, and a liquid Au–In alloy is formed.[30,31] The InP nanowires grown (in the ⟨100⟩ direction) from these particles turned out to have a diameter of 73 ± 4 nm independent of filling time. Assuming that the catalyst composition remains unchanged during the nucleation stage of nanowire growth, we calculated the expected contact angle at the droplet–nanowire interface (β_c) and the expected In fraction of the droplet $(x_{In,c})$ during nanowire growth for all exposure times (Figure 2c, and see Table S1,2 in Supporting Information for more details). Using cross-sectional SEM studies we observed that the Au–In particles sink into the substrate during the annealing step. Therefore, the volume underneath the substrate was also taken into account in the calculation (Figure S1, Supporting Information).

In order to obtain the actual indium concentration during growth, the sample was cooled down under arsine (AsH_3) instead of PH_3 at the end of the growth time. During this process an InAs segment is formed, consuming the indium present in the catalyst droplet during InP nanowire growth. The amount of indium in both the InAs segment and the Au–In droplet is quantified after growth by energy dispersive X-ray analysis (EDX) in the TEM (see inset of Figure 2c) to

Figure 3. (a,d) SEM images of InP nanowires grown on InP (100) substrate with growth direction changing (a) from ⟨100⟩ to ⟨111⟩ after 2 min indium depletion and (d) from ⟨100⟩ to ⟨111⟩ and back to ⟨100⟩; (b,e) zoom-in images of (a,d) respectively. Image (b) is viewed with 85° tilt angle and images (a), (d), and (e) with 30°. (c,f) Bright-field TEM images of the nanowires in (b,e), respectively. Both images were acquired slightly off the ⟨011⟩ zone axis in the ⟨100⟩ segments and of the ZB sections in the ⟨111⟩ segments. Off-axis imaging was applied to visualize the stacking faults. The scale bars are 5 μm for panels (a) and (d) and 200 nm for panels (b), (c), (e), and (f). In (c), the lower ⟨100⟩ segment points out of the plane.

determine the contact angle β_a and the indium concentration $x_{In,a}$ during InP nanowire growth (see Supporting Information S2 for more details). The results are shown in Figure 2c by gray (β_a = 125° ± 3°) and blue ($x_{In,a}$ = 0.44 ± 0.03) bands, respectively.

Upon comparing the values for β and x_{In} found by these two methods, it becomes clear that a high vertical yield is obtained if the composition of the catalyst droplet before nanowire growth is already close to the self-stabilized composition during growth. The fact that β_a and $x_{In,a}$ are somewhat smaller than β_c and $x_{In,c}$ after 15 s exposure time is probably due to indium consumption during nucleation, which was not taken into account in the calculation of β_c and $x_{In,c}$.

To illustrate why it is important to have the same catalyst composition during the nucleation stage and during nanowire growth, HCl was used to suppress unwanted lateral growth,[23,32] such that the nanowire bottom part as formed by the VLS mechanism can be studied. One observes that without indium prefilling there are always several stacking faults (SFs) at the bottom of the wires. Importantly, with a filling time of 15 s the nanowire is defect-free (Figure S4, Supporting Information). Stacking faults can be formed in the initial growth stage when the nanowire growth is initiated from a catalyst that is not yet in dynamic equilibrium with the vapor and the solid phase. During this nucleation process the shape of the droplet changes by the uptake of indium, which destabilizes the growth. By prefilling the droplet with indium the catalyst is brought into equilibrium conditions and ⟨100⟩ growth is stabilized. However, if the catalyst is filled with too much indium (e.g., 25 s In filling), it will first kink to one side to release excess material, and then start to grow (Figure S5, Supporting Information), which may explain why the error bar of 25 s filling in Figure 1e is large. This study demonstrates the possibility to define and stabilize the growth direction by engineering the catalyst droplet condition already at the onset of the nucleation event.[33]

Next, the high-yield ⟨100⟩ InP nanowire arrays are used as a template for reversible switching of the growth direction. After

7.5 min of ⟨100⟩ nanowire growth, TMI is switched off for several different time intervals while PH$_3$ is kept on. The wires continue to grow with decreasing indium fraction in the droplet until the indium concentration is below the supersaturation level required for nanowire growth. For indium depletion times longer than 1.5 min, the nanowire growth direction switches from ⟨100⟩ to ⟨111⟩. It can be seen in Figure 3a that almost all wires end with a segment in one of the two symmetrically equivalent ⟨111⟩ crystal directions. A zoom-in of a cross-sectional SEM image is shown in Figure 3b, showing the consistency in growth direction. It should be noted that the switching occurs across the entire substrate with good uniformity. Figure 3c is a bright-field TEM image of one of the nanowires as presented in Figure 3b, showing a defect-free ⟨100⟩ bottom segment and a top part with planar stacking faults (SFs) leading to a ZB/WZ mixed phase. These mixed ⟨111⟩$_{ZB}$/⟨0001⟩$_{WZ}$ segments will be referred to as ⟨111⟩ segments in the rest of this paper. The 55° change in growth direction reflects the single crystalline nature of the transition, the angle being the intrinsic angle between ⟨111⟩ and ⟨100⟩ directions in a cubic lattice.

Finally, we focused on switching back the growth direction from ⟨111⟩ to ⟨100⟩. After growing for 5 min in the ⟨100⟩ and ⟨111⟩ directions consecutively, the PH$_3$ is switched off while TMI is kept on for different periods. During this growth interrupt the indium liberated by TMI decomposition will be collected and absorbed by the catalyst droplet. After the interrupt, the PH$_3$ is switched on for another 5 min before cooling down. About 30% of the wires switches back from ⟨111⟩ to ⟨100⟩ after a 2 min growth interrupt (SEM in Figure 3d). For the majority of these double-kinked wires, the second switching angle is 16° (details in Supporting Information, Figure S6). The minority has a 55° kink, yielding a final ⟨100⟩ segment that is identical in orientation to the first ⟨100⟩ segment, as seen in Figure 3e, selected to highlight the reversible direction switching. The epitaxial relation between the top and bottom ⟨100⟩ segments of the latter type is
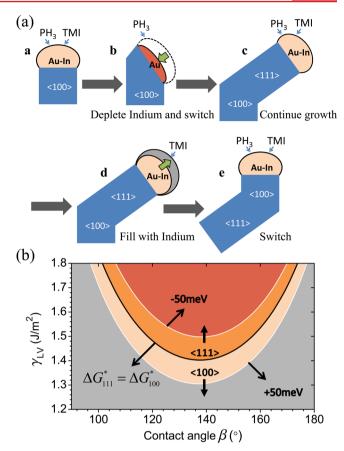
illustrated by the identical fast Fourier transforms (FFT) of the high-resolution TEM (HRTEM) images of top and bottom segments (Figure S7, Supporting Information). Figure 3f displays that the $\langle 100 \rangle$ top segment is free of stacking faults. In the lower part of this top segment, sets of $\{111\}$ twin planes are present in the three symmetrically equivalent directions, all being inclined to the growth direction. The kinking angle, that is, 16 or 55°, is determined by the number of twin boundaries at the second switching junction from $\langle 111 \rangle$ to $\langle 100 \rangle$ (see Supporting Information S3 for more details). About 70% of the nanowires continues growth in the $\langle 111 \rangle$ direction during the change in droplet volume (Figure S6b,d, Supporting Information). The local increase in thickness of these nanowires halfway the $\langle 111 \rangle$ segment reflects the stage in the growth process in which the droplet volume was increased by additional filling with indium.[34] In general, our approach shows the possibility of making reversible switching of growth directions in single InP nanowire with proper modulation of the indium concentration in the catalyst droplet. This method can be tested for a variety of other materials. Correspondingly, the change of catalyst droplet and its effect on nanowire growth direction is shown schematically in Figure 4a.

The influence of the composition of the catalyst droplet on the nanowire growth direction may be understood semi-quantitatively from the nucleation kinetics of layer-by-layer VLS growth for which Glas et al.[35] have put forward a basic description, which has been used successfully in several quantitative nanowire growth models.[35−39] Adapting this kinetic nucleation model to the present situation, we calculate the Gibbs free energy ΔG_i^* of nucleation for both nanowire growth directions, and by comparing these two values, determine which growth direction is preferred (see Supporting Information S4 for more details). The difference of these Gibbs free energies, $\Delta G_{111}^* - \Delta G_{100}^*$, is plotted as a function of the liquid−vapor surface energy, γ_{LV}, and the droplet−nanowire contact angle, β, in Figure 4b. For large γ_{LV}, generally $\Delta G_{111}^* < \Delta G_{100}^*$ and $\langle 111 \rangle$ is the preferred growth direction, while the opposite holds for small γ_{LV}. This result of the model is robust, meaning that it does not change qualitatively with different assumptions on the shape of the nucleus and the value of the solid−liquid surface energy, although the precise position of the borderline between $\langle 111 \rangle$ and $\langle 100 \rangle$ does (see S6 in Supporting Information).

Since the liquid−vapor surface energy of Au is much larger (1.22 J/m^2)[40] than that of In (0.54 J/m^2),[41] the upper (lower) part of the figure corresponds to low (high) indium fraction in the catalyst droplet. The model explains qualitatively that InP nanowires can grow in either $\langle 100 \rangle$ or $\langle 111 \rangle$ direction under similar growth conditions, and that growth can be reversibly switched between the two directions by changing the indium concentration in the catalyst particle. It reproduces the tendency to grow in the $\langle 100 \rangle$ direction for high indium concentration and in the $\langle 111 \rangle$ direction for a depleted catalyst. In the model, it is implicitly assumed that the growth process occurs in thermal equilibrium, whereas in reality it is at the most stationary. Most likely, there are energy barriers to overcome during switching from $\langle 100 \rangle$ to $\langle 111 \rangle$ and vice versa, which would introduce hysteresis effects. A more detailed understanding of preferential nanowire growth directions would require additional investigations of the switching dynamics but this is beyond the scope of the present paper.

We have demonstrated the growth of gold-catalyzed $\langle 100 \rangle$ InP nanowire arrays on InP (100) substrate with a high vertical

Figure 4. (a) The change of catalyst droplet shape with indium filling/depleting during nanowire growth and the effect on wire growth direction. [a] InP nanowire growing in the $\langle 100 \rangle$ direction catalyzed by the Au−In alloy droplet using TMI and PH$_3$ as precursors. [b] Indium in the droplet is depleted when TMI is switched off, and the growth direction changes from $\langle 100 \rangle$ to $\langle 111 \rangle$. [c] The nanowire continues to grow in the $\langle 111 \rangle$ direction with TMI on. [d] PH$_3$ is off and the droplet is filled with indium. [e] The nanowire changes growth direction from $\langle 111 \rangle$ back to $\langle 100 \rangle$ and continues to grow in the $\langle 100 \rangle$ direction with PH$_3$ on. (b) Contour plot of $\Delta G_{111}^* - \Delta G_{100}^*$ versus γ_{LV} and β, indicating the favorable growth direction of InP nanowires, which is $\langle 111 \rangle$ when $\Delta G_{111}^* < \Delta G_{100}^*$ and is $\langle 100 \rangle$ when $\Delta G_{111}^* > \Delta G_{100}^*$.

yield. We found that a high yield can be obtained by filling the catalyst droplet with indium prior to the nanowire growth. Importantly, the highest yield is obtained when the droplet composition prior to the growth corresponds to the particle composition during nanowire growth. Reversible switching of the nanowire growth direction has been realized using catalyst engineering. Switching of the nanowire growth direction may create new opportunities to realize novel nanoscale devices.[42,43]

■ ASSOCIATED CONTENT

Ⓢ Supporting Information
Additional information, figures, and tables. This material is available free of charge via the Internet at http://pubs.acs.org.

■ AUTHOR INFORMATION

Corresponding Author
*E-mail: e.p.a.m.bakkers@tue.nl.

Notes
The authors declare no competing financial interest.

REFERENCES

(1) Duan, X. F.; Huang, Y.; Cui, Y.; Wang, J. F.; Lieber, C. M. *Nature* **2001**, *409*, 66.

(2) Wang, J.; Gudiksen, M. S.; Duan, X.; Cui, Y.; Lieber, C. M. *Science* **2001**, *293*, 1455.

(3) Pettersson, H.; Trägårdh, J.; Persson, A. I.; Landin, L.; Hessman, D.; Samuelson, L. *Nano Lett.* **2006**, *6* (2), 229.

(4) Yan, R.; Gargas, D.; Yang, P. *Nat. Photonics* **2009**, *3*, 569.

(5) Wallentin, J.; Anttu, N.; Asoli, D.; Huffman, M.; Åberg, I.; Magnusson, M. H.; Siefer, G.; Fuss-Kailuweit, P.; Dimroth, F.; Witzigmann, B.; Xu, H. Q.; Samuelson, L.; Deppert, K.; Borgström, M. T. *Science* **2013**, *339*, 1057−1060.

(6) Wagner, R. S.; Ellis, W. C. *Appl. Phys. Lett.* **1964**, *4*, 89.

(7) Trentler, T. J.; Hickman, K. M.; Goel, S. C.; Viano, A. M.; Gibbons, P. C.; Buhro, W. E. *Science* **1995**, *270*, 1791.

(8) Persson, A. I.; Larsson, M. W.; Stenström, S.; Ohlsson, B. J.; Samuelson, L.; Wallenberg, L. R. *Nat. Mater.* **2004**, *3*, 677.

(9) Wu, Z. H.; Mei, X.; Kim, D.; Blumin, M.; Ruda, H. E.; Liu, J. Q.; Kavanagh, K. L. *Appl. Phys. Lett.* **2003**, *83*, 3368.

(10) Ghosh, S. C.; Kruse, P.; LaPierre, R. R. *Nanotechnology* **2009**, *20*, 115602.

(11) Mikkelsen, A.; Sköld, N.; Ouattara, L.; Lundgren, E. *Nanotechnology* **2006**, *17*, S362.

(12) Fortuna, S. A.; Wen, J.; Chun, I. S.; Li, X. *Nano Lett.* **2008**, *8*, 4421.

(13) Inari, M.; Takeda, J.; Motohisa, J.; Fukui, T. *Physica E* **2004**, *21*, 620.

(14) Ikejiri, K.; Ishizaka, F.; Tomioka, K.; Fukui, T. *Nano Lett.* **2012**, *12* (9), 4770.

(15) Poole, P. J.; Lefebvre, J.; Fraser, J. *Appl. Phys. Lett.* **2003**, *83*, 2055.

(16) Wacaser, B. A.; Deppert, K.; Karlsson, L. S.; Samuelson, L.; Seifert, W. *J. Cryst. Growth* **2006**, *287*, 504.

(17) Givargizov, E. I. *Cryst. Growth* **1975**, *31*, 20.

(18) Zhang, X.; Zou, J.; Paladugu, M.; Guo, Y.; Wang, Y.; Kim, Y.; Joyce, H. J.; Gao, Q.; Tan, H. H.; Jagadish, C. *Small* **2009**, *5*, 366.

(19) Givargizov, E. I. *Krist. Tech.* **1975**, *10*, 473−484.

(20) Bjork, M. T.; Ohlsson, B. J.; Sass, T.; Persson, A. I.; Thelander, C.; Magnusson, M. H.; Deppert, K.; Wallenberg, L. R.; Samuelson, L. *Appl. Phys. Lett.* **2002**, *80*, 1058−1060.

(21) Krishnamachari, U.; Borgstrom, M.; Ohlsson, B. J.; Panev, N.; Samuelson, L.; Seifert, W.; Larsson, M. W.; Wallenberg, L. R. *Appl. Phys. Lett.* **2004**, *85*, 2077−2079.

(22) Li, Z. A.; Möller, C.; Migunov, V.; Spasova, M.; Farle, M.; Lysov, A.; Gutsche, C.; Regolin, I.; Prost, W.; Tegude, F. J.; Ercius, P. *J. Appl. Phys.* **2011**, *109*, 114320.

(23) Wang, J.; Plissard, S.; Hocevar, M.; Vu, T. T. T.; Zehender, T.; Immink, G. G. W.; Verheijen, M. A.; Haverkort, J.; Bakkers, E. P. A. M. *Appl. Phys. Lett.* **2012**, *100*, 053107.

(24) Tian, B.; Xie, P.; Kempa, T. J.; Bell, D. C.; Lieber, C. M. *Nat. Nanotechnol.* **2009**, *4*, 824−829.

(25) Musin, I. R.; Filler, M. A. *Nano Lett.* **2012**, *12*, 3363−3368.

(26) Diedenhofen, S. L.; Janssen, O. T. A; Grzela, G.; Bakkers, E. P. A. M.; Gómez Rivas, J. *ACS Nano* **2011**, *5*, 2316−2323.

(27) Plissard, S. R.; Slapak, D. R.; Verheijen, M. A.; Hocevar, M.; Immink, G. G. W.; Van Weperen, I.; Nadj-Perge, S.; Frolov, S. M.; Kouwenhoven, L. P.; Bakkers, E. P. A. M. *Nano Lett.* **2012**, *12* (4), 1794−1798.

(28) Pierret, A.; Hocevar, M.; Diedenhofen, S. L.; Algra, R. E.; Vlieg, E.; Timmering, E. C.; Verschuuren, M. A.; Immink, W. G. G.; Verheijen, M. A.; Bakkers, E. P. A. M. *Nanotechnology* **2010**, *21*, 065305.

(29) Plissard, S.; Larrieu, G.; Wallart, X.; Caroff, P. *Nanotechnology* **2011**, *22*, 275602.

(30) Buchan, N. I.; Larsen, C. A.; Stringfellow, G. B. *J. Cryst. Growth* **1988**, *92*, 591−604.

(31) Liu, H. S.; Cui, Y.; Ishida, K.; Jin, Z. P. *CALPHAD: Comput. Coupling Phase Diagrams Thermochem.* **2003**, *27*, 27−37.

(32) Borgström, M.; Wallentin, J.; Trägårdh, J.; Ramvall, P.; Ek, M.; Wallenberg, L.; Samuelson, L.; Deppert, K. *Nano Res.* **2010**, *3*, 264−270.

(33) Naji, K.; Dumont, H.; Saint-Girons, G.; Penuelas, J.; Patriarche, G.; Hocevar, M.; Zwiller, V.; Gendry, M. *J. Cryst. Growth* **2012**, *343*, 101−104.

(34) Crawford, S.; Lim, S. K.; Gradecak, S. *Nano Lett.* **2012**, *13*, 226−232.

(35) Glas, F.; Harmand, J. C.; Patriarche, G. *Phys. Rev. Lett.* **2007**, *99*, 146101.

(36) Algra, R. E.; Verheijen, M. A.; Borgström, M. T.; Feiner, L. F.; Immink, G.; van Enckevort, W. J. P.; Vlieg, E.; Bakkers, E. P. A. M. *Nature* **2008**, *456*, 369−72.

(37) Dubrovskii, V. G.; Sibirev, N. V.; Harmand, J. C.; Glas, F. *Phys. Rev. B* **2008**, *78*, 235301.

(38) Algra, R. E.; Verheijen, M. A.; Feiner, L. F.; Immink, G. G. W.; Theissmann, R.; van Enckevort, W. J. P.; Vlieg, E.; Bakkers, E. P. A. M. *Nano Lett.* **2010**, *10*, 2349−2356.

(39) Joyce, H. J.; Wong-Leung, J.; Gao, Q.; Tan, H. H.; Jagadish, C. *Nano Lett.* **2010**, *10*, 908−915.

(40) Egry, I.; Lohoefer, G.; Jacobs, G. *Phys. Rev. Lett.* **1995**, *75*, 4043.

(41) McClelland, M. A.; Sze, J. S. *Surf. Sci.* **1995**, *330*, 313−322.

(42) Tian, B. Z.; Cohen-Karni, T.; Qing, Q.; Duan, X. J.; Xie, P.; Lieber, C. M. *Science* **2010**, *329*, 830−834.

(43) Xu, L.; Jiang, Z.; Qing, Q.; Mai, L.; Zhang, Q.; Lieber, C. M. *Nano Lett.* **2013**, *13* (2), 746−751.